JOURNAL OF POLYMER SCIENCE | PART B

Polymer Physics

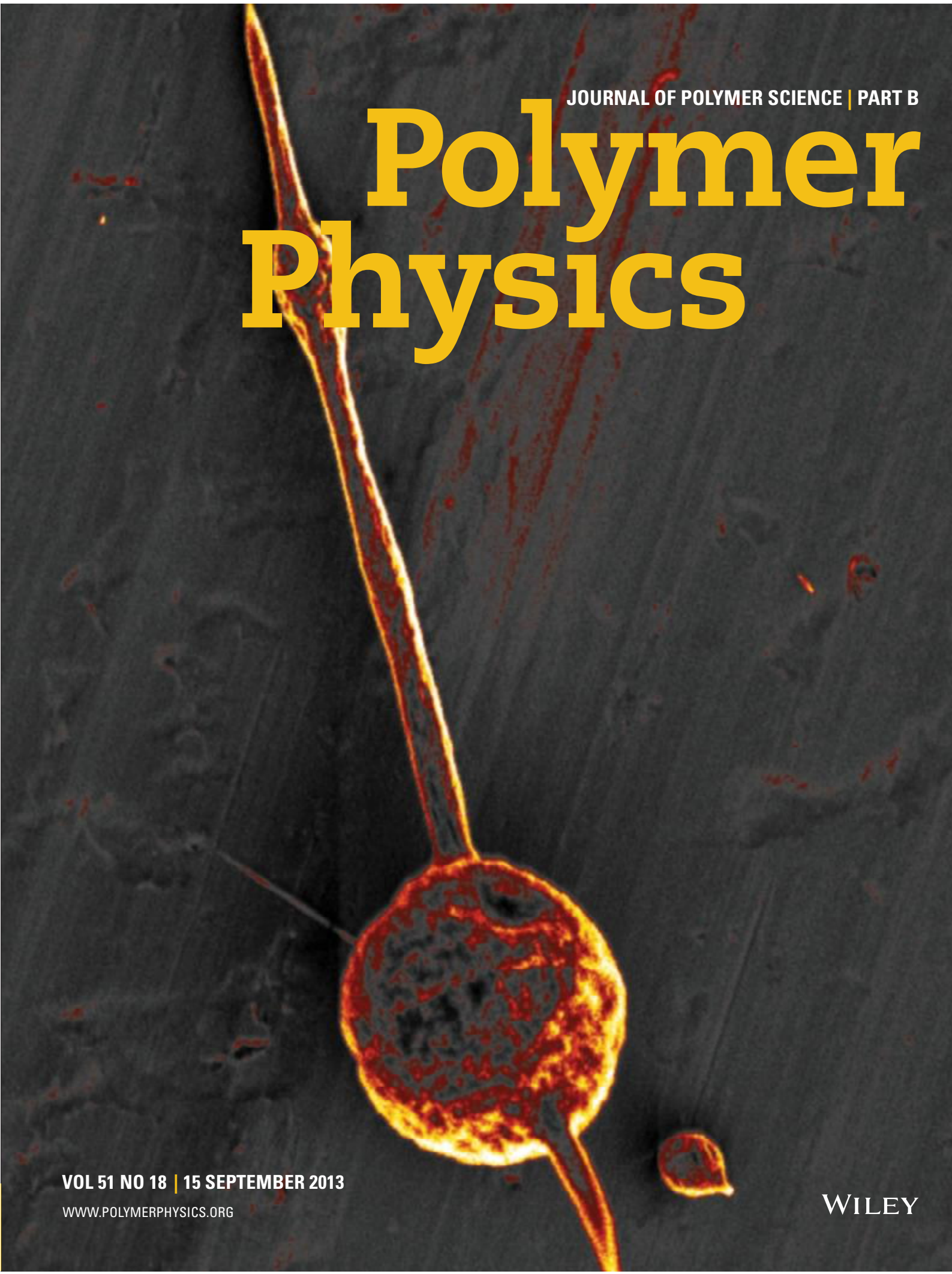

VOL 51 NO 18 | 15 SEPTEMBER 2013
WWW.POLYMERPHYSICS.ORG
WILEY

WWW.POLYMERPHYSICS.ORG

JOURNAL OF POLYMER SCIENCE | PART B

Polymer Physics

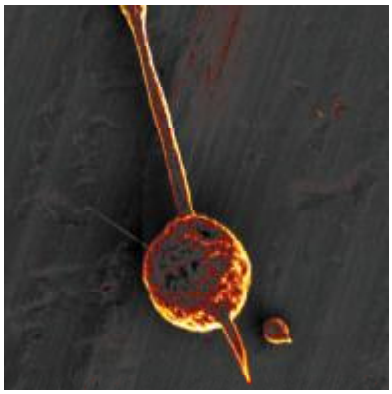

ELECTROSPINNING

Electrospinning of a semi-dilute polymer solution can yield short nanofibers of submicrometer diameter. The short nanofiber shown on the cover is 500 nm in diameter and 30 mm in length, and has a bead-on-string structure. Identified by Israel Greenfeld and Eyal Zussman on page 1377 as the outcome of polymer entanglement loss caused by the strong extensional flow of electrospinning, short nanofibers are promising as compact, aligned, rigid nanostructures, with possible applications in tissue engineering, drug delivery, composite reinforcement, filtration, electrical and thermal conduction, and light amplification.

Polymer Entanglement Loss in Extensional Flow: Evidence from Electrospun Short Nanofibers

Israel Greenfeld, Eyal Zussman

Department of Mechanical Engineering, Technion - Israel Institute of Technology, Haifa 32000, Israel
Correspondence to: I. Greenfeld (E-mail: green_is@netvision.net.il)

Received 24 May 2013; revised 16 June 2013; accepted 17 June 2013; published online 17 July 2013
DOI: 10.1002/polb.23345

ABSTRACT: High strain rate extensional flow of a semidilute polymer solution can result in fragmentation caused by polymer entanglement loss, evidenced by appearance of short nanofibers during electrospinning. The typically desired outcome of electrospinning is long continuous fibers or beads, but, under certain material and process conditions, short nanofibers can be obtained, a morphology that has scarcely been studied. Here we study the conditions that lead to the creation of short nanofibers, and find a distinct parametric space in which they are likely to appear, requiring a combination of low entanglement of the polymer chains and high strain rate of the electrospinning jet. Measurements of the length and diameter of short nanofibers, electrospun from PMMA dissolved in a blend of $CHCl_3$ and DMF, confirm the theoretical prediction that the fragmentation of the jet into short fibers is brought about by elastic stretching and loss of entanglement of the polymer network. The ability to tune nanofiber length, diameter and nanostructure, by modifying variables such as the molar mass, concentration, solvent quality, electric field intensity, and flow rate, can be exploited for improving their mechanical and thermodynamic properties, leading to novel applications in engineering and life sciences. © 2013 Wiley Periodicals, Inc. J. Polym. Sci., Part B: Polym. Phys. **2013**, *51*, 1377–1391

KEYWORDS: beads; disentanglement; electrospinning; fibers; fracture; networks; nanotechnology; nanofibers; inorganic polymers; jet; PMMA; short nanofibers; viscoelastic properties

INTRODUCTION The high strain rate of an extensional flow, such as the flow of an electrospinning semidilute polymer solution jet, can result in fragmentation as a consequence of loss of the polymer network entanglement, leading to appearance of short nanofibers varying from a few tens of nanometers to a few microns in diameter. Short nanofibers are a unique morphology of electrospun polymeric nanofibers, in addition to the continuous nanofibers and nanobeads morphologies. Typically, long continuous nanofibers or beads are the preferred outcome in electrospinning applications, while short nanofibers are an undesirable defect. However, electrospun short polymeric nanofibers are expected to find important applications in engineering and life sciences.[1] Although short nanofibers can be produced by methods such as solution precipitation[2] or ultrasonication of continuous fibers,[3] their creation by electrospinning without any post-processing offers unique structures and enhanced mechanical properties.

Discontinuous beaded fibers and elongated beads are known to appear in low-concentration solutions, when the concentration is sufficiently high to avoid excessive dilution and creation of beads from droplets.[4–6] By gradually increasing the concentration, continuous fibers begin to appear. Bead-free short fibers with aspect ratios of 10–200 were obtained by varying the polymer–solvent system and molecular weight.[1] Polymer entanglement was identified as the key factor affecting the transition from the bead morphology, through that of elongated beads or short fibers, to that of continuous fibers.[1,4,6]

Short nanofibers have been scarcely explored, and further study is needed to measure the dominant factors that influence their creation and properties. Furthermore, the nanoscale mechanism that leads to short nanofiber formation requires clarification, particularly with regards to how disentanglement initiates the fragmentation of the electrospinning jet.

Short nanofibers can be created in a semi–dilute entangled solution, depending on the polymer architecture (linear or branched), molar mass, solution concentration and solvent quality. Generally, at given electric field intensities and flow rates, lower concentrations and poorer solvents decrease chain entanglement, and consequently increase the likelihood that short nanofibers will appear during electrospinning (Fig. 1). Also, short nanofibers are frequently accompanied by beads-on-string and free beads [Fig. 1(b,d)], a phenomena associated with low viscosity and high surface tension.

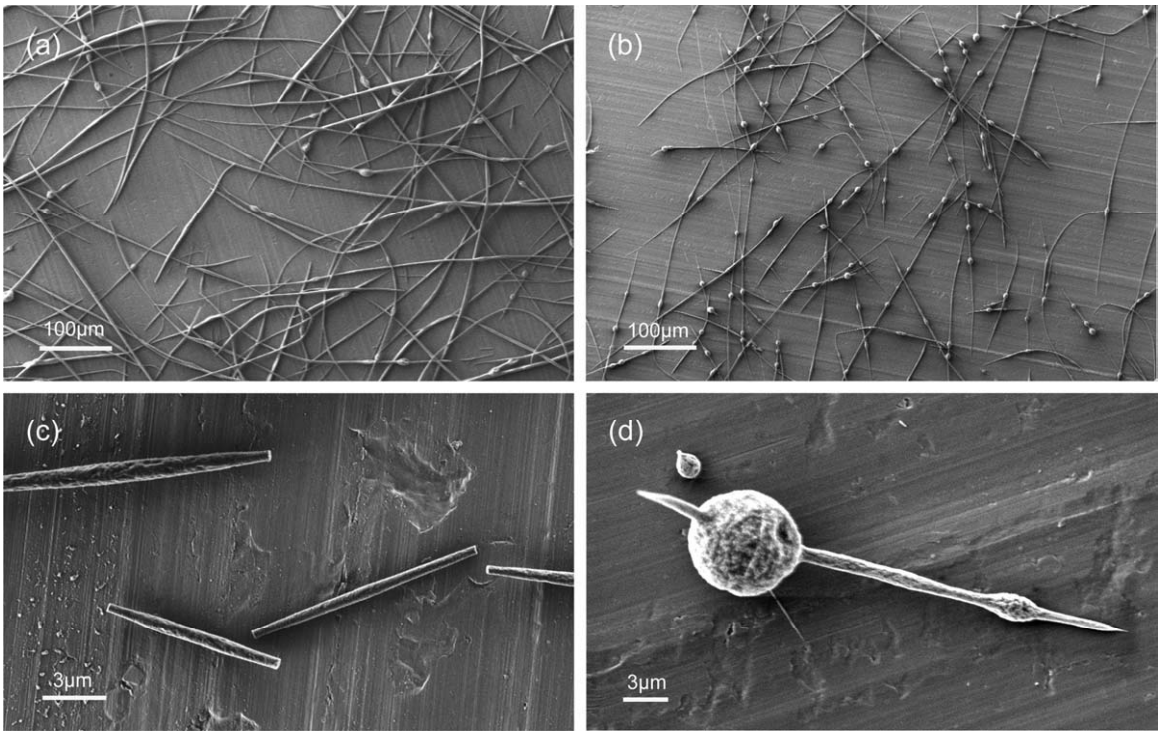

FIGURE 1 SEM micrographs of electrospun short nanofibers, with (right) and without (left) beads-on-string. Electrospinning conditions: molar mass 15 kDa PMMA, electric field 0.75 kV/cm, and flow rate 1 mL/h. Polymer concentration (vol %)/$CHCl_3$:DMF solvent composition (vol %) were: (a) 31.3/70:30, (b) 32.2/50:50, (c) 29.3/50:50, and (d) 27.5/30:70.

When the polymer network is not highly entangled, the high strain rate caused by the electrostatic field can stretch and disentangle chains from the network, and break the jet into short segments. Entanglement loss is governed by two opposing variables, both dependent on the degree of polymerization N of the polymer chain. The entanglement number, the number of topological constraints along the chain, scales with N, while the chain relaxation time in an entangled network scales with N^3. When the jet strain rate is low, rapid relaxation of the network prevents entanglement loss and viscosity is dominant. However, at high strain rates, relaxation is not sufficiently fast and elasticity is dominant, making chain extension and disentanglement possible. Hence, lower N (shorter chain) reduces entanglement, but at the same time reduces relaxation time; thus, the net effect on entanglement loss relies upon the strain rate.

At the same time, the rapid solvent evaporation characteristic of electrospinning partially solidifies the jet, sometimes creating a solid skin,[7–9] and retards entanglement loss and jet breaking, but also prevents the jet segments from contracting back into droplets by relaxation and surface tension. Electrospinning involves many material, process and ambient variables that impact the final outcome; for the purpose of this study, we chose to focus on those affecting entanglement and strain rate.

We electrospun PMMA, a linear thermoplastic polymer, dissolved in a solvent blend of $CHCl_3$ and DMF, at semi–dilute concentrations slightly above the entanglement concentration. By tuning the process and material parameters, a distinct, albeit small, parametric space where short nanofibers appeared was clearly identified, and its boundaries with the other electrospun morphologies (continuous fibers, beads-on-string, and beads) were defined. The proposed disentanglement mechanism that leads to jet fragmentation was substantiated by examining SEM images of fiber fractures and by measuring the parametric dependence of the length and diameter of short nanofibers. Further substantiation was obtained by theoretical predictions that describe the entanglement loss process, assuming known jet rheology and affine extension of the polymer network. The experimental and theoretical investigations focused on the control of the molar mass, concentration, solvent quality, electric field, and flow rate variables, and correlated well over a wide parametric space.

EXPERIMENTAL

Materials and Methods

Electrospinning was carried out by pumping a polymer solution into a syringe, and drawing it by a strong electric field toward a collector. The polymer solution was injected into a capillary needle using a syringe pump, at flow rates ranging from 0.1 to 2 mL/h. The solutions were drawn by an electric potential of 4.5 to 50 kV, across a needle-collector (upper-lower electrodes) gap that was adjusted between 4 and 30

TABLE 1 Properties of Tested Polymer and Solvents[a]

Polymer	ρ [g/cm^3]	M_w [Da][b]	M_w [Da][c]	M_n [Da][c]	$Đ$
PMMA	1.20	15,000	12,700	10,100	1.26
PMMA	1.20	101,000	82,300	43,600	1.89
PMMA	1.20	350,000	288,400	162,500	1.77

Solvent	ρ[g/cm^3]	M_w [Da]	η_s [mPa s]	γ [mN/m][d]	σ[mS/m]	χ
DMF	0.95	73	0.92	37	0.25	1.16 [f]
$CHCl_3$	1.48	119	0.54	27	0.002 [e]	0.44 [e]

[a] Density ρ, weight-average molar mass M_w, number-average molar mass M_n, dispersity $Đ=M_w/M_n$, zero-shear solvent viscosity η_s, surface tension γ, electrical conductivity σ, and Flory's interaction parameter χ (with PMMA).
[b] Manufacturer's data.
[c] GPC results.
[d] Ref. 10. Surface tension measurements (Wilhelmy method) of PMMA 15 kDa dissolved in $CHCl_3$:DMF 50:50 vol % resulted in 32.7 ± 0.5 mN/m over a wide range of concentrations.
[e] Ref. 11
[f] Mark.[12]
[g] Selvakumar et al.[13]

cm, yielding an average electric field of 0.6–6.2 kV/cm. The collector was a wheel of 20-cm diameter, rotating at tangential speeds of up to 26 m/s. Samples were collected on aluminum foils placed on the wheel edge and on glass slides close to the wheel, and were imaged by scanning electron microscopes (resolution down to 3 nm/pixel) and an optical microscope (resolution down to 0.4 μm/pixel), respectively. Under certain material and process conditions, the jet fragmented and short nanofibers were collected. The experiments were conducted at a temperature of 25 ± 1.2 °C, and at a relative humidity of $50 \pm 10\%$.

The polymer, PMMA (poly(methyl methacrylate)) purchased from Sigma-Aldrich, came in three different molar masses (15, 101, and 350 kDa). PMMA is a transparent thermoplastic polymer (T_g=105°C), with a tensile strength of 70 N/mm^2, and is brittle in its pure composition at room temperature. The solvents were a blend of $CHCl_3$ (chloroform) and DMF (dimethyl formamide), at volume ratios between 0:100 and 70:30 vol %. The polymer was dissolved in the solvent blend, at concentrations varying between 3 and 40 wt %. The relevant properties of the polymer and solvents are presented in Table 1.

To avoid over-parameterization, the electric field intensity and polymer concentration were used as free parameters, while the other parameters were assigned the following nominal conditions: solvent composition $CHCl_3$:DMF 50:50 vol %, flow rate 1 mL/h, collector velocity 2.8 m/s, and gap distance between the electrodes 10 cm. These nominal conditions were modulated within a limited range to assess their influence as well. The polymer concentration c was selected so that the solution would be within the semi–dilute entangled regime, generally with a relative concentration c/c_e (c_e is the entanglement concentration) between 1 and 2, a range in which chain entanglement is fairly low but still spinnable. This range is known as a transition zone between beads and continuous fibers, producing a mixture of nanobeads, nanofibers, and elongated beads.[4] The current work shows that, under certain conditions, solutions in this relative concentration range yield short nanofibers as well. The overlap concentration c^* and the entanglement concentration c_e for each molar mass were obtained by measuring the solution specific viscosity as a function of the polymer concentration (Appendix A), and are presented in Table 2.

TABLE 2 Measured Overlap and Entanglement Concentrations for PMMA Dissolved in $CHCl_3$:DMF 50:50 vol %[a]

M_w [kDa]	c^* [g/mL]	φ^* [vol %]	c_e [g/mL]	ϕ_e [vol%]
15	0.086	7.2	0.254	21.2
101	0.039	3.2	0.118	9.8
350	0.019	1.6	0.058	4.8

[a] Molar mass M_w, overlap concentration c^*, overlap volume fraction φ^*, entanglement concentration c_e, and entanglement volume fraction ϕ_e. Calculated from the measured viscosity by intersecting the power fit curves of adjacent concentration regimes (Appendix A), and using $\varphi=c/\rho$. Estimated accuracy is ±10%.

The ratio between the entanglement concentration and the overlap concentration is similar for the three molar masses, $\phi_e/\phi^* \cong 3$ (expressing the concentration in terms of the volume fraction $\varphi=c/\rho$). The dependence of ϕ_e on the degree of polymerization N (in terms of Kuhn monomers, $N=M_w/598$ for PMMA) was obtained by power fitting the results from Table 2:

$$\phi_e \approx N^{-0.46}, \quad (1)$$

compared to theoretical predictions of $N^{-0.75}$ for θ-solvent and $N^{-0.76}$ for a good solvent.[14]

Jet and Fiber Fragmentation

Short nanofibers form when the jet breaks into fragments before complete solvent evaporation and fiber solidification (Fig. 2). The fragmentation of the jet can be viewed on both the macroscopic and microscopic scales. Macroscopically, the tensile stress continuously grows along the jet, and is larger when the electric field intensity is higher. The stress in an electrically driven fluid jet is generated by the electrostatic force applied on charged ionic species, which are induced into the electrically conductive fluid by the electric field. The stress in the jet is proportional to sE, where E is the electrostatic field intensity, and s is the surface density of the electric charge. At the free end of the jet the stress is zero, but at a distance x from the free end it is proportional to E^2x^2,[15] giving rise to a viscoelastic stress that scales with E^2.

Eventually, if the stress exceeds the jet tensile strength, the jet will break at weak points [Fig. 2(a)]. At the break point, the stress is fully relieved, but is gradually restored upstream to the breakpoint until, sufficiently far from the

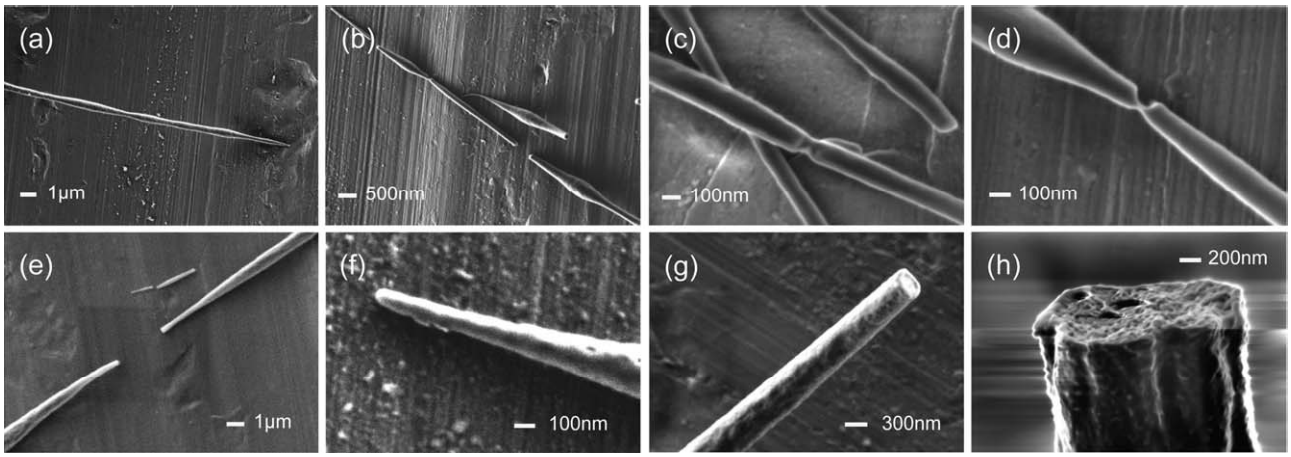

FIGURE 2 SEM micrographs of short nanofibers formation: (a) Diameter fluctuations. (b) Fragmentation. (c) Necking. (d) Break. (e) Separated fragments. (f) Round tip. (g) Fractured tip. (h) Fracture surface.

break, the effect of the break on the stress in the jet is no longer significant. As a result, the next break occurs at a distance from the previous break point, creating a fragment—a short nanofiber—and, when repeated, a sequence of fragments [Fig. 2(b)]. This mechanism is analogous to the fragmentation of a rigid fiber embedded in a soft matrix under tension (Cox and Kelly-Tyson models),[16,17] in which the fiber stress is proportional to the interfacial stress between the matrix and the fiber, and rises linearly with the distance from the break. In the Cox model, the fragment length is proportional to the fiber strength and inversely proportional to the interfacial stress. The analogy to jet fragmentation is attained by replacing the fiber strength by a power of the entanglement number, and the interfacial stress by E^2.

Typical breaking starts with necking [Fig. 2(c)] that gradually increases [Fig. 2(d)] until full break [Fig. 2(e)]. Since pure PMMA is brittle in its solid state, the presence of necking confirms that fragmentation occurs while the jet has not yet fully solidified, and material flow is still possible. The fragment tip is typically round [Fig. 2(f)], but sometimes, when solidification is more advanced, the fiber ultimately breaks in a cohesive facture [Fig. 2(g,h)].

Fragmentation of the liquid jet can be explained by a microscopic-scale mechanism. An extensional flow of a polymer solution induces hydrodynamic forces on the polymer network, resulting in stretching of the network.[18] Chains disentangle from the polymer network in fast extensional flows such as electrospinning, by a dynamic process involving stretching, reptation along an effective confining tube, and relaxation.[4,19–22] The entanglement loss is faster when the flow's strain rate is high, the chains are short, and the polymer concentration is low. Eventually, chains can detach from the network, leading to the network's complete separation. Upon separation, the tension in chains close to the break is relieved, and their relaxation leads to regaining some of the lost entanglement. As the stress, and consequently the disentanglement, is gradually restored far from the break, the next break point occurs at a distance from the previous break point. In addition, network entanglement heterogeneities, due to local variations in the polymer degree of polymerization and solution concentration, may cause jet failure.

The evolution of the axial stress and the entanglement number (number of entanglements along the chain) is schematically illustrated in Figure 3. The mechanism is repetitive, and therefore the length and diameter of the created short nanofibers should be consistent for given conditions. The cyclic nature of the entanglement number lies at the base of the diameter fluctuations seen in Figure 2(a), which are macroscopically explained by axisymmetric Rayleigh instability of highly conducting, viscoelastic polymer solutions,[23–26] leading to a wavy contour and formation of beads.

Hence, it is suggested that jet fragmentation is caused by disentanglement of chains, to the extent that the network loses its continuity and breaks up at intervals. Such breaking can only be experimentally observed if the entanglement loss is

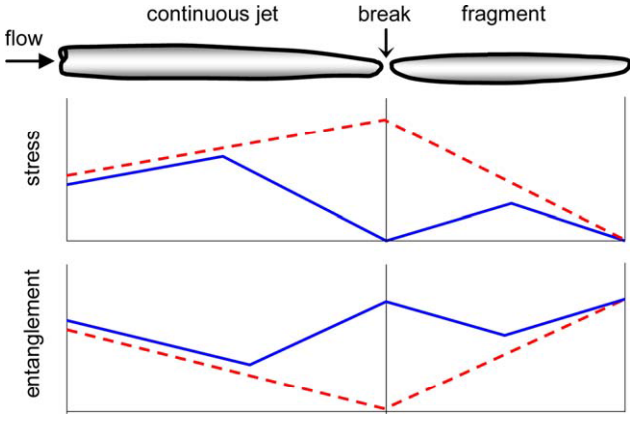

FIGURE 3 Illustration of the proposed evolution of the jet's axial stress and entanglement number (number of entanglements along the chain), before (dashed line) and after (solid line) jet break. [Color figure can be viewed in the online issue, which is available at wileyonlinelibrary.com.]

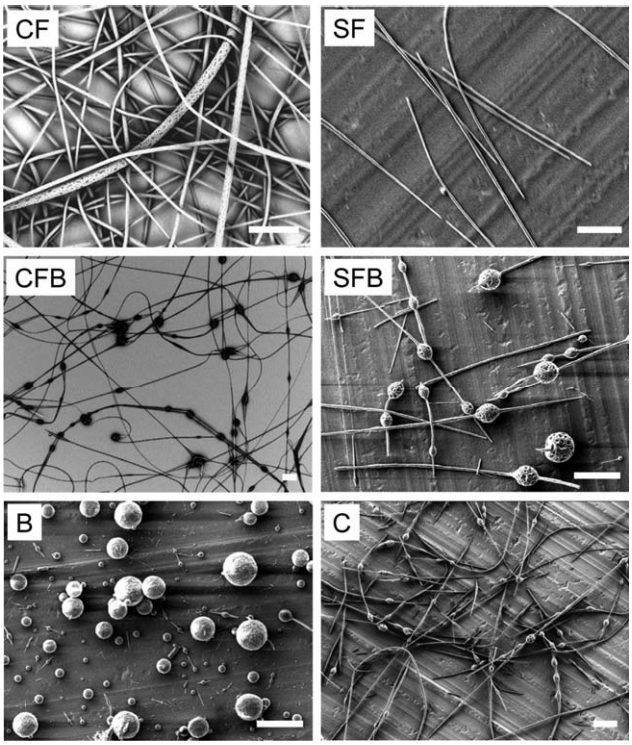

FIGURE 4 Representative SEM micrographs of the distinct nanofiber morphology regions: continuous fibers (CF), short fibers (SF), beads on continuous fibers (CFB), beads on short fibers (SFB), beads (B), and transition (mixed morphologies) (C). The scale bars are 20 μm.

fully completed within the gap between the needle and the collector. This mechanism, described in detail in the Theoretical Section, offers a good explanation for the necking and breaking process, as well as reasonable theoretical predictions for the process and material dependence of short nanofiber features.

Occurrence of Short Nanofibers and Beads

Overall, 76 experiments at varying electrospinning parameters were run, out of which 38 experiments produced short nanofibers. The observed morphologies can be categorized to continuous fibers, short fibers, beads on continuous fibers, beads on short fibers, and stand-alone beads, as shown in Figure 4. Under transitional conditions, mixed morphologies were observed.

The data set of the tests run under the nominal conditions (see Materials and Methods Section) is depicted in Figure 5, mapping the occurrence of the different morphologies as a function of the electric field intensity E and the polymer volume fraction φ normalized by a power of the degree of polymerization N. The exponents of N were tuned until the best separation between the morphology regions was achieved, enabling estimation of the boundaries by power curves. The following trends are observed for the occurrence of short nanofibers [Fig. 5(a)]. At a given molar mass (i.e., N), short nanofibers occur at lower concentration and higher electric field. As the molar mass is increased, short nanofibers are less frequent or do not appear at all. At molar mass of 350 kDa short nanofibers only appeared when a lower $CHCl_3$:DMF ratio was used. In terms of the proposed microscopic mechanism, chains are more likely to disentangle completely when they are shorter (lower molar mass), when the polymer network is less entangled because of low concentration and/or poorer solvent (causing chains to contract), and when the external electrostatic force is higher.

Beads-on-string occur at lower concentration and molar mass as well [Fig. 5(b)]. However, contrary to short nanofibers, beads-on-string occur at low electric field intensity, when the surface tension is strong enough to overcome the viscous forces driven by the electrostatic tension. Standalone beads appear as the concentration is reduced, particularly below the entanglement concentration φ_e. The boundary of the beads-on-string region is expressed by two power curves with different slopes: the upper curve relates to beads on

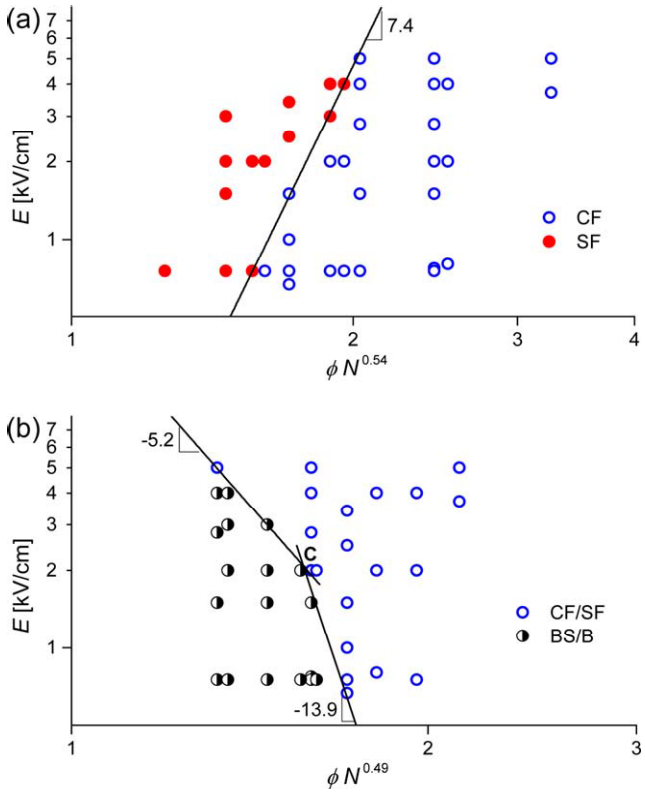

FIGURE 5 Occurrence of short fibers (a) and beads-on-string (b) in electrospun PMMA dissolved in $CHCl_3$:DMF 50:50 vol %. The flow rate was 1 mL/h and the molar mass was 15,000, 101,000, and 350,000 Da. The morphology regions are mapped over the electric field E, the polymer volume fraction ϕ, and the degree of polymerization N. The boundaries between the regions are depicted by power curves. Estimated accuracy of exponents: ±10%. Point C in (b) marks the transition from the electrostatic regime (upper section) and the viscoelastic regime (lower section)—explained in the text. [Color figure can be viewed in the online issue, which is available at wileyonlinelibrary.com.]

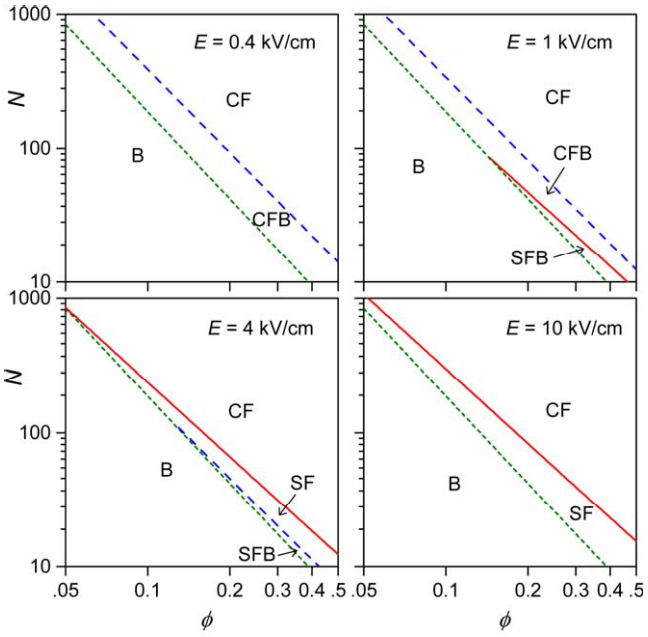

CF continuous fibers, SF short fibers, CFB beads on continuous fibers, SFB beads on short fibers, B beads

FIGURE 6 Generalized plot of the morphology regions, based on the experimental data set of Figure 5, mapped over the degree of polymerization N and the polymer volume fraction ϕ, for four different values of the electric field E. The lines correspond to eqs 1 and 2. [Color figure can be viewed in the online issue, which is available at wileyonlinelibrary.com.]

short fibers while the lower curve relates to beads on continuous fibers. Indeed, two different mechanisms are involved, since with continuous fibers the surface tension stress is opposed by the viscoelastic stress in the jet, while in short fibers the jet is fragmented and the opposing stress is electrostatic. As the electrostatic stress is lower than the viscoelastic stress, beading is more likely to occur in short fibers, as observed in the test results. Further analysis of the beading mechanism is beyond the scope of this article, as this issue has been broadly investigated both experimentally and theoretically.[4,23–25,27,28]

The morphology boundaries measured in Figure 5 can be used to formulate the electrospinning conditions for occurrence of short nanofibers (SF), beads on short fibers (SFB), and beads on continuous fibers (CFB):

$$\begin{aligned} &E^{-1}N^{4.0}\phi^{7.4} < \text{const.} \quad \text{SF} \\ &\text{EN}^{2.5}\phi^{5.2} < \text{const.} \quad \text{SFB} \\ &\text{EN}^{6.7}\phi^{13.9} < \text{const.} \quad \text{CFB}, \end{aligned} \tag{2}$$

when all the other process and material parameters that determine the constants are kept unchanged. These equations are depicted in Figure 6, together with eq 1 that marks the boundary of the standalone beads region. Note that the short fibers region is a fairly narrow strip that disappears completely at the low value of the electric field intensity (upper-left pane). The acceptable working ranges for E, N, and φ necessary for jetting are not shown. Obviously, the borderlines between the regions are not as sharp as shown, but a clear picture emerges, depicting distinct morphologies and respective process and material conditions that lead to them.

Equation 2 can be expressed in terms of the relative concentration ϕ/ϕ_e, using the measured molar mass dependence of the entanglement concentration ϕ_e from eq 1:

$$\begin{aligned} &E^{-1}N^{0.6}(\phi/\phi_e)^{7.4} < \text{const.} \quad \text{SF} \\ &EN^{0.1}(\phi/\phi_e)^{5.2} < \text{const.} \quad \text{SFB} \\ &EN^{0.3}(\phi/\phi_e)^{13.9} < \text{const.} \quad \text{CFB}. \end{aligned} \tag{3}$$

These conditions are not entirely dependent on the number of entanglements n_e along the chain (theoretically[14] $n_e \approx (\phi/\phi_e)^{1.3}$), as they depend on N and E as well. In other words, the shorter the chain and the less it is entangled, the entanglement loss will be faster and the likelihood of short nanofibers and beads-on-string will be higher. These equations are depicted in Figure 7, where E/N^{α} is plotted as a function of the relative concentration. The plot details may vary for different data sets (different polymer, solvent, jet initial velocity, etc.), but the overall layout of the plot is universal. For example, better solvent quality (higher $CHCl_3$:DMF ratio) increases entanglement and will therefore pull the plot upward. The effect of additional parameters is addressed in the next sections. Note that short fibers can only occur at normalized

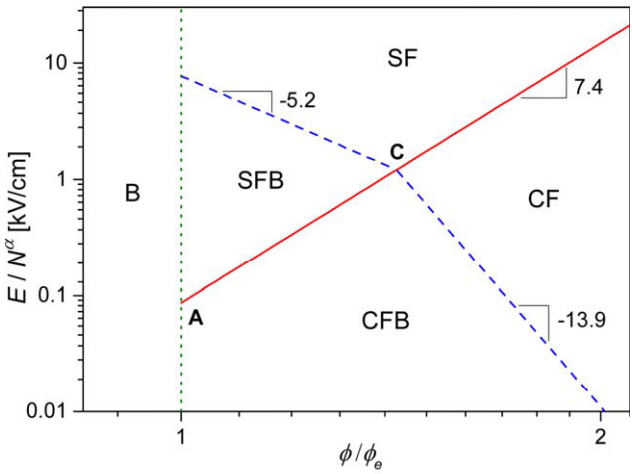

CF continuous fibers, SF short fibers, CFB beads on continuous fibers, SFB beads on short fibers, B beads, C transition point

FIGURE 7 Universal plot of the morphology regions, based on the experimental data set of Figure 5, mapped over the electric field E and the relative polymer concentration φ/φ_e. E is normalized by N^{α}, where N is the degree of polymerization and α is 0.6 (solid line), −0.1 (upper dashed line), and −0.3 (lower dashed line). The lines correspond to eq 3. [Color figure can be viewed in the online issue, which is available at wileyonlinelibrary.com.]

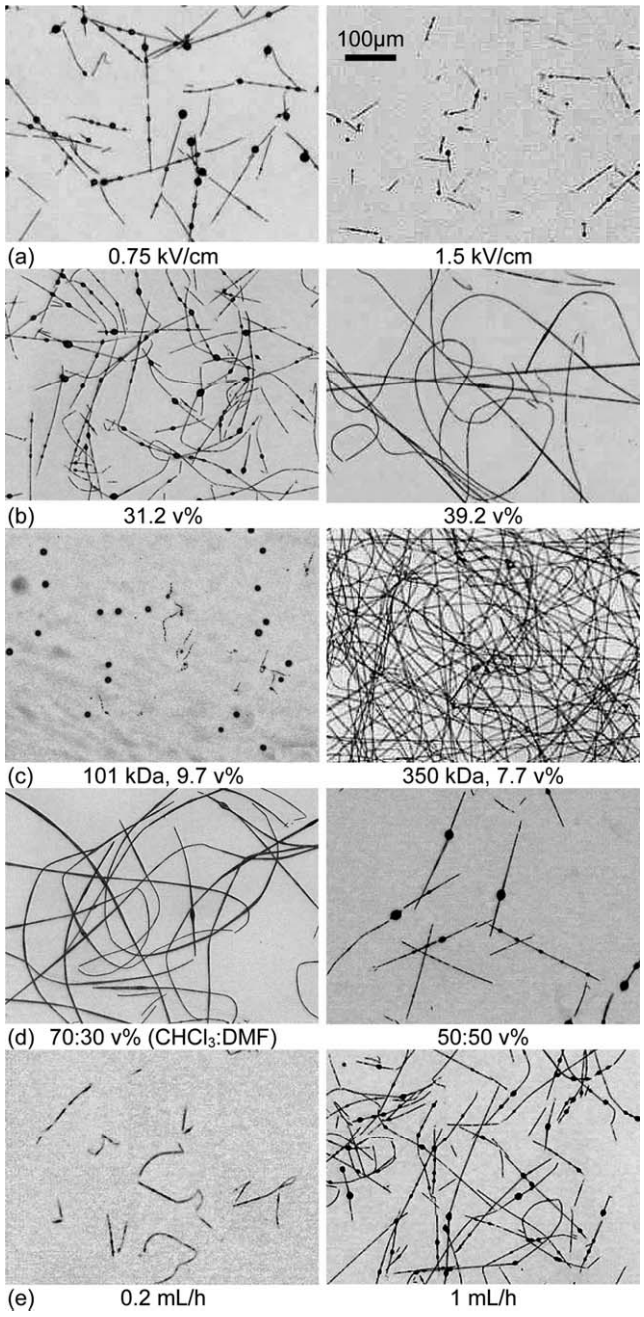

FIGURE 8 Effect of solution properties and process parameters on short nanofiber length (optical micrographs): (a) electric field (15 kDa, $CHCl_3$:DMF 50:50 vol %, 1 mL/h, 29.3 vol %), (b) polymer concentration (15 kDa, 50:50 vol %, 1 mL/h, 2 kV/cm), (c) molar mass (50:50 vol %, 0.75 kV/cm, 1 mL/h), (d) DMF fraction (15 kDa, 1 mL/h, 0.75 kV/cm, 31.2 vol %), and (e) flow rate (15 kDa, 50:50 vol %, 2 kV/cm, 31.2 vol %).

electric field intensity above point A, and short fibers without beads can occur only above the transition point C.

Short Nanofiber Length and Diameter

When the conditions for short nanofibers are met, the fragment length is the most distinctive property. The length depends on the material and process parameters, as demonstrated in Figure 8. Generally, the fragment length is shorter upon increasing the electric field intensity [Fig. 8(a)], decreasing the polymer concentration [Fig. 8(b)], decreasing the molar mass [Fig. 8(c)], decreasing the $CHCl_3$:DMF ratio [Fig. 8(d)], and decreasing the flow rate [Fig. 8(e)]. In line with the proposed entanglement loss mechanism, all of these conditions contribute to rapid chain disentanglement, and consequently to shorter fiber fragments. The polymer network is less entangled for shorter chains, lower concentrations, and poorer solvents (e.g., lower $CHCl_3$:DMF ratio), while higher electric field intensities and lower feed velocities increase the extensional strain rate, together leading to more rapid disentanglement and shorter fiber fragments. When the parametric conditions are reversed, the fragment length will increase, until continuous fibers are restored at the boundary described in the previous section. Note the randomly oriented scattering of fragments on the revolving collector, seen in Figure 8, which indicates that fragmentation occurs before reaching the collector, during the free flight of the jet.

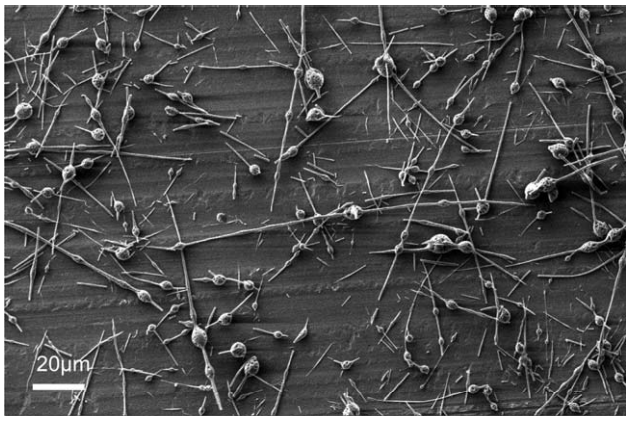

FIGURE 9 SEM micrograph demonstrating the dispersity of short nanofiber lengths and diameters. Conditions: molar mass 15 kDa, polymer concentration 29.3 vol %, solvents composition $CHCl_3$: DMF 50:50 vol %, electric field 3 kV/cm, and flow rate 1 mL/h.

The tested samples yielded short nanofibers of lengths ranging from 1 to 1000 μm and of diameters ranging from 50 nm to 3 μm. When observing a representative experimental sample in the image of Figure 9, and its length and diameter measurements in Figure 10(a), it becomes clear that even when all material and process parameters are fixed, the dispersion of fragment lengths and diameters is high, correlating well with lognormal distribution[1] [Fig. 10(b)]. Tiny fragments are by far more frequent than large fragments, and therefore, the number-average (mean) length L_n and diameter D_n are biased downward and their measurement is not stable. Instead, we use the weight-average length and diameter, $L_w = \sum L_i^2 / \sum L_i$ and $D_w = \sum D_i^2 / \sum D_i$ (analogous to the weight-average molar mass M_w), which give a higher weight to larger fragments. As shown further on, the experimental material and process dependencies match well with the weight-average length and diameter. Note that the fragment aspect ratio rises with fragment length [inset of Fig. 10(a)].

One is tempted to associate the high dispersity of fragment sizes with the fairly high molar mass dispersity of the polymer

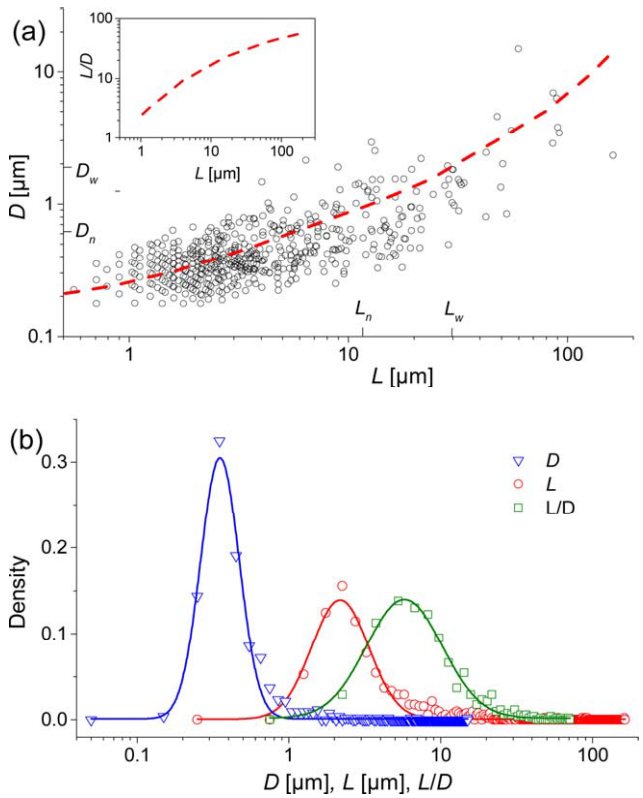

FIGURE 10 Example of the dispersity of short nanofiber lengths L, diameters D, and aspect ratios L/D. The measurements were taken from the SEM micrograph of Figure 9. (a) Measured diameter and length of the fragments. The number-average (L_n, D_n) and weight-average (L_w, D_w) values are indicated on the axes. The dispersity is $Đ_L = L_w/L_n = 2.7$ and $Đ_D = D_w/D_n = 3.1$. The inset shows the measured aspect ratio. The correlation between L and D is >0.6. (b) Distribution density of diameter, length and aspect ratio, with lognormal fit. [Color figure can be viewed in the online issue, which is available at wileyonlinelibrary.com.]

used in the experiment (Table 1), but the average molar mass at different jet cross sections should not diverge significantly. Rather, large fluctuations in the local jet diameter, due to the jet's dynamic instability, splitting and branching,[29] as well as local concentration variations, due to rapid solvent evaporation, are more likely to spawn such size dispersity.

The dependence of the length and diameter on the material and process parameters was analyzed for the experimental data sets in Table 3, all of which yielded short nanofibers. Variations were applied to the molar mass, flow rate, solvents ratio, electric field intensity, and polymer concentration. The fragments weight-average length varied over a wide range of 10^1–10^3 μm, whereas the diameter varied within a much narrower range of 0.7–3 μm.

Dependence of the fragment length and diameter on the electric field is estimated by power fitting of the data from samples in which only the electric field intensity was modified [Fig. 11(a)]. Similarly, the concentration dependence is

TABLE 3 Experimental Data Sets Used for Diameter and Length Measurements[a]

M_w [kDa]	Q [mL/h]	$CHCl_3$:DMF [vol%]	E [kV/cm]	φ [vol%]
15	1	50:50	2	39.2
|	|	|	|	32.2
|	|	|	|	31.2
|	|	|	|	29.3
|	|	|	3	|
|	|	|	1.5	|
|	|	|	0.75	|
|	|	|	|	31.2
|	|	|	|	32.2
|	|	|	|	34.2
|	|	30:70	2	27.5
|	|	|	0.75	|
|	|	70:30	|	31.3
|	|	0:100	|	29.8
|	|	|	2	|
|	0.2	50:50	|	31.2
|	|	|	3	|
|	|	30:70	0.75	27.5
|	2	70:30	2	31.3
|	|	|	4	|
101	1	50:50	|	14.6
|	|	|	3	|
|	|	|	0.75	9.7
350	|	0:100	|	3.2
|	|	|	4	|

[a] Weight-average molar mass M_w, flow rate Q, solvent volume ratio $CHCl_3$:DMF, electric field E, and polymer volume fraction φ.

estimated by power fitting of samples in which only the concentration was modified, separately for two values of electric field intensity [Fig. 11(b)]. The dependence on the other three parameters (molar mass, flow rate, and solvent ratio) was estimated by multivariate power fitting of the data, using the already estimated electric field and concentration exponents from Figure 11.

The results of the length power fit are combined in the following scaling expression:

$$L_{\mathrm{FIT}} \approx v_0^{1.4} E^{-1.1} N^{3.9} \kappa^{2.1} \phi^{7.5}, \tag{4}$$

where v_0 is the jet initial velocity, E is the applied electric field, κ is the solvents blend quality, N is the degree of polymerization, and ϕ is the polymer volume fraction. Similarly, the results of the diameter power fit are combined in the following scaling expression:

$$D_{\mathrm{FIT}} \approx v_0^{0.1} E^{-0.07} N^{-0.4} \kappa^{-0.2} \phi^{0.19}. \tag{5}$$

Note that v_0 substitutes the flow rate Q, considering that the experiments were carried out with a fixed needle internal

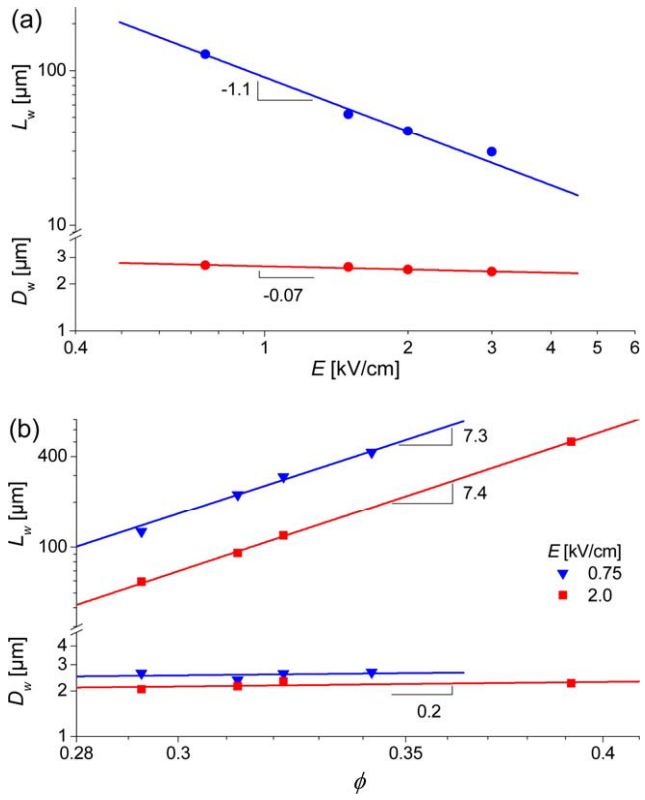

FIGURE 11 Short nanofiber weight-average length L_w and diameter D_w, measured for molar mass 15,000 kDa, flow rate 1 mL/h, and $CHCl_3$:DMF ratio 50:50 vol %. Power fit curves and corresponding exponents are shown. (a) Length and diameter *versus* the electric field E, for polymer concentration 29.3 vol %. (b) Length and diameter *versus* the polymer volume fraction φ, for two cases of electric field. Based on the experimental data sets of Table 3. [Color figure can be viewed in the online issue, which is available at wileyonlinelibrary.com.]

diameter. The solvents blend quality is approximated by the dimensionless term $\kappa=(2\chi-1)^{-1}$, where χ is the concentration-weighted interaction parameter of the two solvents with the polymer, $\chi=\phi_{DMF}\chi_{DMF}+(1-\phi_{DMF})\chi_{CHCl3}$ (ϕ_{DMF} is the DMF volume fraction in the solvents blend). The values of χ_{DMF} and χ_{CHCl3} are given in Table 1. Figure 12 demonstrates the quality of the power fit and confirms the scaling approach, which is further validated by the analysis in the next section.

Higher v_0 and lower E result in a reduced velocity gradient and therefore longer L, while they have a negligible effect on D. Higher κ (better solvent blend - higher $CHCl_3$:DMF ratio) result in longer L and smaller D. The solvent quality dependence of L is apparent, as a better solvent increases chain swelling and consequently entanglement, resulting in slower entanglement loss and longer fragments. However, the solvent quality dependence of D is opposite; when the network is more entangled, due to a better solvent, its extension ratio upon breaking is higher, and therefore its condensed diameter is smaller.

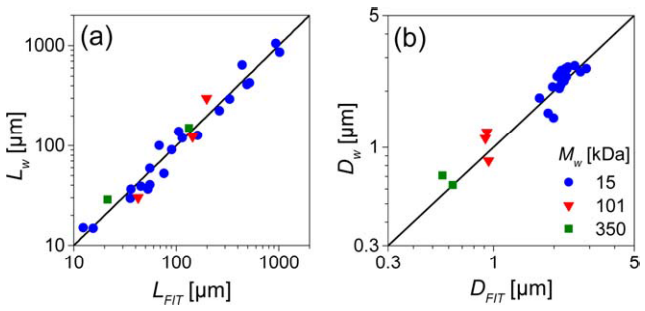

FIGURE 12 Measured weight-average short nanofiber length L_w (a) and diameter D_w (b), *versus* the corresponding power-fit curves L_{FIT} (eq 4) and D_{FIT} (eq 5). Based on the experimental data sets of Table 3. [Color figure can be viewed in the online issue, which is available at wileyonlinelibrary.com.]

Writing eqs 4 and 5 in terms of the relative concentration ϕ/ϕ_e, using eq 1 (omitting all other terms):

$$L_{FIT} \sim N^{0.5}(\phi/\phi_e)^{7.5}$$
$$D_{FIT} \sim N^{-0.5}(\phi/\phi_e)^{0.19}, \quad (6)$$

we observe that higher entanglement number $n_e \approx (\phi/\phi_e)^{1.3}$ yields larger L due to increased viscosity and reduced velocity gradient, and that L increases with the degree of polymerization N. The shorter the chain and the less it is entangled, the more rapid entanglement loss will be, and fragment lengths will be consequentially shorter. The effect of N on the diameter is opposite, as a longer chain means higher chain extensibility, whereas the effect of n_e is minor. In contrast, the diameter of continuous fibers is highly dependent on n_e, as will be shown in the next section.

The upper limit of the fragment length L scales with the gap distance between the electrodes d [Fig. 13(a)], and therefore eq 4 can be used to define the condition for the occurrence of short nanofibers:

$$Kd > v_0^{1.4}E^{-1.1}N^{3.9}\kappa^{2.1}\phi^{7.5}, \quad (7)$$

where K is a constant prefactor. This equation compares well with the boundary of short nanofibers occurrence of eq 2, const. $> E^{-1}N^{4.0}\phi^{7.4}$, which was derived in a completely different way. Moreover, since the occurrence boundary scales with the position at which the jet separates, z_s [Fig. 13(a)], this observation leads to the conclusion that the short nanofiber length should be proportional to the breaking position, $L \sim z_s$, even though their orders of magnitude may be quite disparate. This result is used in the next section for estimating the fragment length (eq 15).

THEORETICAL DESCRIPTION

Disentanglement of Polymer Chains

The highly entangled polymer network within the electrospinning semidilute solution ensures the continuity of the jet and the eventual formation of continuous nanofibers. As suggested, the occurrence of short nanofibers is brought about

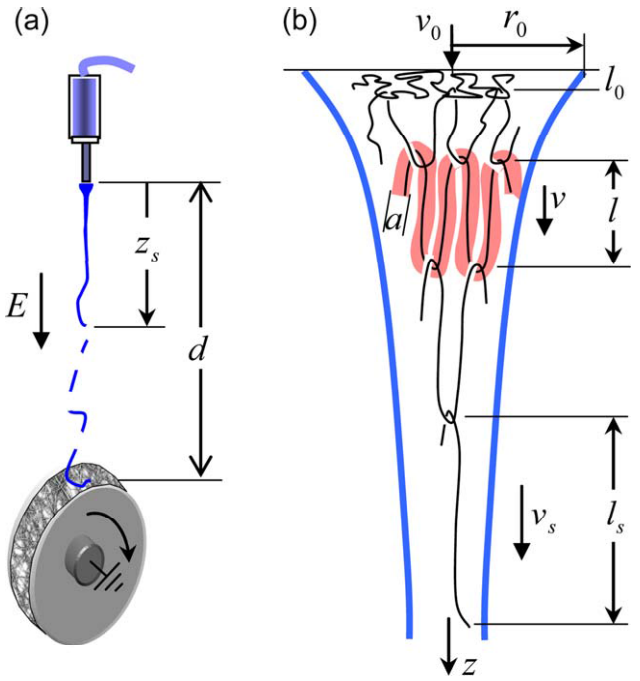

FIGURE 13 Illustration of electrospinning and jet fragmentation (a), and network disentanglement (b). The blue (outer) curves in (b) are the jet boundary, and the pink (thick) curve represents the confining tube. Elastic extension of chains, followed by stress relief resulting from chain reptation along a confining tube, gradually disentangle chains from the network. The subscript *s* denotes the jet break point. [Color figure can be viewed in the online issue, which is available at wileyonlinelibrary.com.]

by substantial entanglement loss during the electrospinning process. The entanglements, topological constraints that prevent intercrossing of chains, effectively divide each polymer chain into entanglement strands, which are elastically extended under the applied extensional forces. At equilibrium, chains can reptate within a confining tube, which represents the constraining potential of nearby chains on the strand, allowing monomers to fluctuate within its confining diameter. Under strain, chains can relieve the high elastic tension by sliding along the tube, and be partially disentangled from the network. When the jet strain rate is sufficiently high and the chain relaxation time is sufficiently slow, the chains cannot effectively relax back to their network equilibrium state. Under such conditions, the end-to-end distance of strands will gradually increase, and the number of entanglements along chains will be reduced, eventually resulting in a complete separation of the network and breaking of the jet. The process is illustrated in Figure 13.

The analysis assumes an affine deformation of the polymer network, namely, that the relative extension of each strand is the same as the relative extension of the jet at the same axial position. Thus, the entanglement nodes are supposedly moving at the same velocity as the jet, with negligible local velocity lag or lead with respect to the jet. This approach is reminiscent of the affine tube model of rubber elasticity, except that the contour length of strands is not fixed, but rather increases in consequence of chain sliding along the confining tube. Thus, the extended length of the strand is the result of both elastic stretching and disentanglement. Using this concept, an extended strand having a distance l between its two entanglements, located at a jet position z and axial velocity v, is extended at a velocity of

$$\frac{dl}{dt} \approx l\frac{dv}{dz} \approx \frac{l}{v}\frac{dv}{dt}, \tag{8}$$

or, by rearranging the terms, $\dot{l}/l \approx \dot{v}/v$. Integrating and setting the initial strand length $l_0 = a$ (a is the tube diameter) and the initial jet velocity v_0:

$$\frac{v}{v_0} \approx \frac{l}{l_0} = \frac{l}{a}. \tag{9}$$

A similar expression was obtained by dynamic modeling of network stretching during electrospinning,[18] assuming rubber elasticity with a fixed strand contour length.

Jet Breaking

At the jet start, when the solution is almost at rest, the initial strand length (end-to-end distance) is equivalent to the chain's confining tube diameter, and is given by $a \approx bN_{e1}^{1/2}\phi^{-\nu/(3\nu-1)}$ for an athermal solvent and $a \approx bN_{e1}^{1/2}\phi^{-2/3}$ for a θ-solvent.[14] b is the Kuhn monomer length, N_{e1} is the number of Kuhn monomers in an entanglement strand in the melt (a fixed value for a given polymer, of order 10^0–10^1), ϕ is the polymer volume fraction, and $\nu \cong 0.588$ is the swelling exponent for a good solvent. As a result of the high strain rate, the strand approaches full extension close to the jet start,[18] and, since the strain rate is not relieved throughout the jet, the strand retains a high extension even after partial disentanglement and relaxation. Under such conditions, the end-to-end distance of a strand consisting of N_e monomers can be approximated by $l \cong bN_e$. At low strain rates and fast relaxation times, the strand length may be shorter, or $l \cong bN_e^x$, where $\nu < x < 1$; however, for simplicity, in the following analysis we assume full extension. Thus, upon complete chain disentanglement at jet position z_s, the strand approaches the length of the entire chain, $l_s \cong bN$, and the corresponding jet velocity v_s from eq 9 is:

$$\frac{v_s}{v_0} \approx \frac{l_s}{a} \approx \frac{N}{N_{e1}^{1/2}} \begin{cases} \phi^{\frac{\nu}{3\nu-1}} & \text{athermal solvent} \\ \phi^{2/3} & \theta\text{-solvent.} \end{cases} \tag{10}$$

To obtain a length scale for the network separation, the velocity profile $v(z)$ should be specified. Theoretical and experimental analyses of electrically driven fluid jets have shown that the jet velocity, sufficiently far from the jet start, assumes an asymptotic profile that can be expressed by a power law of the position z along the jet.[30–35] For example,

$$\frac{v}{v_0} \cong k^2\left(\frac{z}{r_0}\right)^{2\beta}, \tag{11}$$

where k is a dimensionless parameter, of order 10^{-1}–10^1, that determines the scale of velocity increase, r_0 is the initial jet radius, of order 10^{-1} mm, and β is an exponent shown to

vary between 0.25 and 1 (β=0.5 is used throughout the rest of the analysis)[30].

The dependence of the flow parameter k on the material and process parameters, can be estimated by substituting the velocity gradient from eq 11, which scales as $\nabla v \sim (v_0/r_0)k^2$, by the strain rate, which scales as $\dot{\varepsilon} \sim E^2/\eta$, yielding $k \sim r_0^{1/2}\eta^{-1/2}v_0^{-1/2}E$. A theoretical derivation based on jet rheology yields $k \cong \varepsilon_m^{1/6}r_0^{2/3}\sigma^{1/4}\eta^{-5/12}v_0^{-2/3}E^{5/6}$ (in CGS electrostatic units), where $\varepsilon_m \cong 1$ is the permeability of the medium (air).[34,35] Substituting the solution viscosity $\eta \cong \eta_s\eta_{sp}$ ($\eta >> \eta_s$, where η_s is the solvent viscosity and η_{sp} is the solution specific viscosity), the flow parameter may be redefined as $k=k_0\eta_{sp}^{-5/12}$. Thus, the jet breaking position, or the jet axial position at which disentanglement is completed, z_s, can be expressed as a function of the corresponding jet velocity v_s:

$$\frac{z_s}{r_0} \approx k^{-2}\frac{v_s}{v_0} \approx k_0^{-2}\eta_{sp}^{5/6}\frac{l_s}{a}$$
$$k_0 \cong \varepsilon_m^{1/6}r_0^{2/3}\sigma^{1/4}\eta_s^{-5/12}v_0^{-2/3}E^{5/6}. \quad (12)$$

Using the known expressions for the viscosity of a semidilute solution,[14] $\eta_{sp} \approx (N^3/N_{e1}^2)\phi^{3/(3\nu-1)}$ for an athermal solvent and $\eta_{sp} \approx (N^3/N_{e1}^2)\phi^{14/3}$ for a θ-solvent, and substituting l_s/a from eq 10, the breaking position is:

$$\frac{z_s}{r_0} \approx k_0^{-2}\frac{N^{7/2}}{N_{e1}^{13/6}}\begin{cases}\kappa^{\frac{17(2\nu-1)}{2(3\nu-1)}}\phi^{\frac{2\nu+5}{2(3\nu-1)}} & \text{good solvent}\\ \phi^{41/9} & \theta\text{-solvent}.\end{cases} \quad (13)$$

Note that the expression is expanded to good solvents by incorporating the dimensionless term κ=v/b^3 (v is the excluded volume), which expresses the solvent quality based on the interaction between monomers in a given solvent; this term rises as the solvent improves, up to the athermal limit where it is equal to 1.

The analysis assumes a homogenous polymer network. Local variations in polymer concentration and deformation, and the dispersity of the polymer degree of polymerization, can influence the results. Discussion on the effects of deformation, disentanglement and evaporation on the solution viscosity, which are not accounted for in the current theoretical analysis, is provided in Appendix B.

Short Nanofiber Occurrence and Length

The jet position z_s where the polymer network separates marks the location where short nanofibers are being created. If $z_s > d$ (d is the gap distance between the electrodes), the jet will not fragment and the nanofibers will be continuous, whereas when $z_s < d$ short nanofibers will appear. Hence, the condition for occurrence of short nanofibers is:

$$\frac{d}{r_0} > \frac{z_s}{r_0}, \quad (14)$$

where z_s is given by eq 13.

Upon breaking, the jet tensile stress at position z_s is relieved, but is gradually restored upstream. Chains will partially relax under the reduced stress, and there will be an entanglement gain, consequently delaying the next break point. This mechanism repeats itself, producing a sequence of fragments. The short fiber length L and the jet breaking position z_s scale similarly with the material and process parameters, as shown in the Experimental Section, inferring that L is proportional to z_s:

$$\frac{L}{r_0} \approx \frac{z_s}{r_0}$$
$$\approx \frac{\eta_s^{5/6}v_0^{4/3}}{\sigma^{1/2}r_0^{4/3}E^{5/3}}\frac{N^{7/2}}{N_{e1}^{13/6}}\begin{cases}\kappa^{\frac{17(2\nu-1)}{2(3\nu-1)}}\phi^{\frac{2\nu+5}{2(3\nu-1)}} & \text{good solvent}\\ \phi^{41/9} & \theta\text{-solvent}.\end{cases} \quad (15)$$

where z_s is obtained from eq 13 and k_0 is explicitly written. Since $z_s \sim d \sim 10^2$ mm and $L \sim 10^{-1}$ mm, a constant prefactor of order 10^{-3} should be added. The concentration dependence of L is $\phi^{4.0}$, for a good solvent, and $\phi^{4.6}$, for a θ-solvent, and, with the effect of deformation on the viscosity (Appendix B), $\phi^{5.3}$ and $\phi^{5.7}$, respectively. The solvent quality dependence of L is $\kappa^{2.0}$. These predictions compare reasonably well with the experimental findings in eqs 2, 4, and 7, specifically $L_{FIT} \approx v_0^{1.4}E^{-1.1}N^{3.9}\kappa^{2.1}\phi^{7.5}$. The two main differences between this prediction and the experiment lie in the concentration and the electric field intensity. The exponent of ϕ does not reflect the full effects of deformation, disentanglement and evaporation on the solution viscosity (Appendix B). The jet rheology assumes a uniform electric field,[35] while in reality, the field magnitude and gradient increase sharply close to the syringe and collector, in a manner similar to the electric field generated by two point charges.[36] The fibers' experimental and theoretical lengths are compared in Figure 14(a).

The length is dependent on both the entanglement number of the solution, $n_e \approx (\phi/\phi_e)^{1.3}$, and the degree of polymerization N, as can be seen when expressed in terms of the relative concentration, using the theoretical entanglement concentration[14] $\phi_e \sim N^{1-3\nu}$, for a good solvent, and $\phi_e \sim N^{-3/4}$, for a θ-solvent:

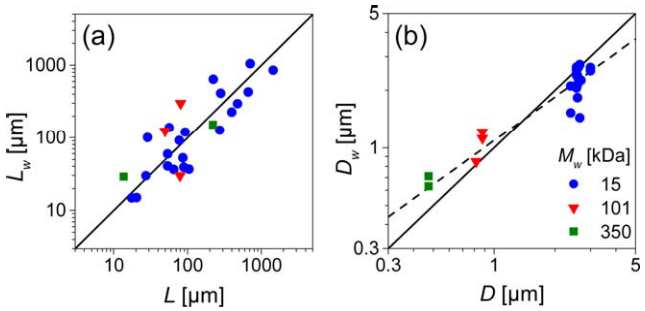

FIGURE 14 Comparison of experimental and theoretical short nanofibers dimensions, based on the experimental data sets of Table 3. The prefactors were adjusted as free parameters. (a) Measured length L_w *versus* the theoretical length L (eq 15). (b) Measured diameter D_w *versus* the theoretical diameter D (eq 18). The dashed line marks the deviation with respect to the molar mass (M_w) dependence, explained in the text. [Color figure can be viewed in the online issue, which is available at wileyonlinelibrary.com.]

$$\frac{L}{r_0} \sim k_0^{-2} \begin{cases} N^{0.41}(\phi/\phi_e)^{4.0} & \text{good solvent} \\ N^{0.08}(\phi/\phi_e)^{4.6} & \theta\text{-solvent}. \end{cases} \quad (16)$$

In line with the analogy to Cox model for the fragmentation of a rigid fiber embedded in a soft matrix under tension, discussed in the Experimental Section, this equation can be reduced to $L \sim n_e^{3.5}/E^{1.7}$ (for a θ-solvent), in which $n_e^{3.5}$ is replaced by the fiber strength and $E^{1.7}$ by the interfacial stress.

Short and Continuous Nanofiber Diameter

Prior to stretching, the condensed polymer network diameter scales with $r_0\sqrt{\phi}$ for initial jet radius r_0. The local condensed diameter, D_c, is reduced by a factor of $\sqrt{l/a}$, as a result of network stretching and disentanglement, and therefore (using eq 9):

$$\frac{D_c}{r_0} \approx \sqrt{\frac{\phi a}{l}} \approx \phi^{1/2}\left(\frac{v}{v_0}\right)^{-1/2}. \quad (17)$$

An alternative expression is $D_c \approx r\sqrt{\phi}$, where r is the local jet radius.

The diameter of short nanofibers can be obtained by inserting the value of l_s/a from eq 10:

$$\frac{D}{r_0} \approx \frac{N_{e1}^{1/4}}{N^{1/2}} \begin{cases} (\phi/\kappa)^{\frac{2\nu-1}{2(3\nu-1)}} & \text{good solvent} \\ \phi^{1/6} & \theta\text{-solvent}. \end{cases} \quad (18)$$

The concentration dependence of short nanofiber diameter is $(\phi/\kappa)^{0.12}$, for a good solvent, and $\phi^{0.17}$, for a θ-solvent. This prediction compares reasonably well with the experimental finding, $D_{FIT} \approx v_0^{0.1}E^{-0.07}N^{-0.4}\kappa^{-0.2}\phi^{0.19}$ (eq. 5). Unlike the length, the theoretical diameter is independent of the jet dynamics (i.e. the initial velocity and electric field). However, the exponents of v_0 and E were not zero in the experiment, implying additional secondary influences. Note the dominance of the degree of polymerization N (larger N leads to smaller D), whereas the other parameters have a weak or null effect. Since the size of a chain (its end-to-end distance) in a semidilute, good-solvent solution is $R \approx bN^{1/2}(\kappa/\phi)^{(\nu-1/2)/(3\nu-1)}$,[14] eq 18 can be written as $D \approx bN_{e1}^{1/4}(r_0/R)$, an inverse dependence of D on R.

The fibers' experimental and theoretical diameters are compared in Figure 14(b). The predicted exponent of N deviates from that obtained from the experiment, as reflected in the dashed line in Figure 14(b). This deviation implies that the entanglement strand does not reach full extension ($l_s \sim N$) upon network separation, as assumed in the theoretical prediction, but rather corresponds to $l_s \sim N^{0.8}$, a substantial extension when compared to the chain's equilibrium end-to-end distance.

In terms of the relative concentration, the short fiber diameter is proportional to:

$$\frac{D}{r_0} \sim \begin{cases} N^{-0.59}(\phi/\phi_e)^{0.12} & \text{good solvent} \\ N^{-0.62}(\phi/\phi_e)^{0.17} & \theta\text{-solvent}. \end{cases} \quad (19)$$

The dependence on N has a negative exponent, as in the experiment, since longer chains allow higher extensibility of the network.

To obtain the diameter of continuous nanofibers, the jet velocity upon reaching the collector is obtained from eq 11 with $z=d$, and is substituted into eq 17:

$$\frac{D}{r_0} \approx k_1^{-1}\frac{N^{5/4}}{N_{e1}^{5/6}} \begin{cases} \kappa^{\frac{15(2\nu-1)}{4(3\nu-1)}}\phi^{\frac{3(2\nu+1)}{4(3\nu-1)}} & \text{good solvent} \\ \phi^{22/9} & \theta\text{-solvent}. \end{cases} \quad (20)$$

where $k_1 = k_0\sqrt{d/r_0}$ and k_0 is defined in eq 12. The concentration dependence of the continuous nanofiber diameter is $\phi^{2.1}$, for a good solvent, and $\phi^{2.4}$, for a θ-solvent, and, with the effect of deformation on the viscosity (Appendix B), $\phi^{2.8}$ and ϕ^3, respectively. The solvent quality dependence of D is $\kappa^{0.9}$. Note that, compared to short nanofibers, the exponent of the degree of polymerization N is positive, (larger N leads to larger D), and that the concentration dependence is much higher, reflecting the dominant effect of the jet dynamics.

In terms of the relative concentration, the continuous fiber diameter is proportional to:

$$\frac{D}{r_0} \sim k_1^{-1} \begin{cases} N^{-0.38}(\phi/\phi_e)^{2.1} & \text{good solvent} \\ N^{-0.58}(\phi/\phi_e)^{2.4} & \theta\text{-solvent}. \end{cases} \quad (21)$$

The results are consistent with the trends in numerous published works, which showed that the diameter of continuous fibers is smaller for lower concentration,[6,37,38] higher electric field intensity,[37,39] lower flow rate,[40] and larger gap distance between the electrodes.[41] More specifically, similar relative concentration dependencies of continuous fiber diameters were measured by Mckee et al.[38] on linear and branched PET-*co*-PEI copolymers and by Gupta et al.[6] on PMMA, yielding $(\phi/\phi_e)^{2.6}$ and $(\phi/\phi_e)^{3.1}$, respectively. These measurements compare well with our theoretical prediction. However, in addition to the dependence on the entanglement number, $n_e \approx (\phi/\phi_e)^{1.3}$, the prediction includes a strong dependence on the degree of polymerization as well, the introduction of which can improve the fit of the data in these references. Furthermore, note that different combinations of material and process variables can lead to the same nanofiber diameter, but with different nanostructure.

The evolution of the fiber length and diameter as a function of the relative polymer concentration is depicted in Figure 15 for a θ-solvent. If $k_1 > 1$ (e.g., low initial velocity, high electric field intensity, and/or large gap distance), short fibers occur and their diameter grows weakly with increasing relative concentration, while their length grows sharply. When the concentration is increased beyond the transition point, $\phi/\phi_e \geq k_1^{0.44}N^{-0.02} \cong k_1^{0.44}$, continuous fibers are created and the diameter growth slope increases abruptly. If $k_1 \leq 1$, only continuous fibers are created. Unlike continuous fibers, the diameter of short fibers is independent of the gap distance between the electrodes d and the parameter k_0 (whose initial velocity and electric field dependencies are

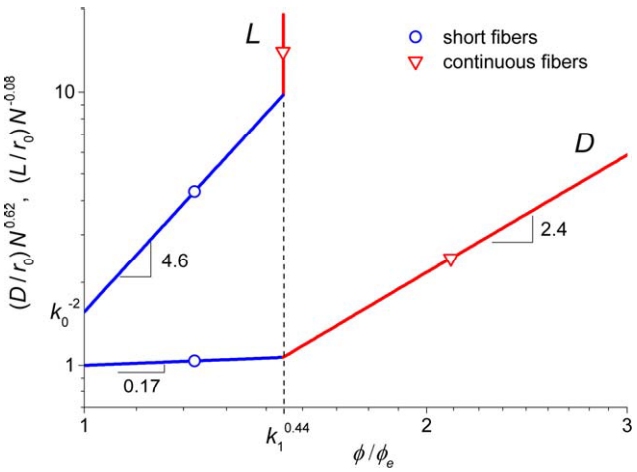

FIGURE 15 Nanofiber length L/r_0 and diameter D/r_0 *versus* the relative concentration φ/φ_e, based on eqs 16, 19, and 21 with approximations (θ-solvent). The length is normalized by $N^{0.08}$ and the diameter by $N^{-0.62}$, where N is the degree of polymerization. Prefactors are ignored. $k_1=k_0\sqrt{d/r_0}$, where the parameter k_0 is defined in eq 12, d is the gap distance between the electrodes, and r_0 is the jet initial radius. The slopes of the two morphology regions—short nanofibers and continuous nanofibers—are marked. [Color figure can be viewed in the online issue, which is available at wileyonlinelibrary.com.]

$\sim v_0^{-2/3}E^{5/6}$). In continuous fibers, the process of disentanglement is not carried out until complete separation of the network, since it is terminated at the collector, and therefore the amount of entanglement loss, and hence the diameter, depend on the flow dynamics and the gap size. In short fibers, once the condition for their occurrence is met, entanglement loss is driven to completion and the diameter is therefore independent of these parameters.

CONCLUSIONS

High strain rate extensional flow of a semidilute polymer solution can result in fragmentation caused by polymer entanglement loss. We found evidence for this phenomenon in the appearance of short nanofibers during electrospinning. Short nanofibers, of lengths ranging from 1 to 1000 μm and of diameters ranging from 50 nm to 3 μm, were electrospun from solutions of PMMA dissolved in a blend of $CHCl_3$ and DMF. The short nanofibers appeared at solution concentrations slightly above the entanglement concentration, when the electric field intensity was high and the flow rate low. When starting from material properties that yield continuous nanofibers, short nanofibers were obtained by decreasing the molar mass, concentration, and solvent quality, all of which contribute to reduced polymer network entanglement. Under such favorable low entanglement and high strain rate conditions, the elastic stretching of the polymer network accelerates the entanglement loss, eventually leading to separation of the network and fragmentation of the jet. The experimental results and theoretical predictions correlate well, confirming the proposed disentanglement mechanism. The analysis identifies the conditions for short nanofiber occurrence, with and without beads-on-string, and explains how their length and diameter depend on the material and process variables.

The high elastic stretching and entanglement loss required to create short nanofibers are likely to lead to an ordered, aligned solid nanostructure with improved mechanical properties. At the same time, since fragmentation occurs before full solidification and collection of the fibers, the polymer network may partially relax in solvent rich areas, and voids may be left in the matrix after evaporation.[9,18,30] A nonuniform structure can result in both the axial and radial directions, with regions of aligned rigid structure and regions of amorphous porous structure. Furthermore, the analysis shows that different combinations of material and process variables can lead to the same nanofiber diameter, but not necessarily to the same internal nanostructure, a result that can be exploited for controlling the mechanical properties.

The ability to tune short nanofiber dimensions can be exploited to improve their as-spun mechanical and thermodynamic properties, such as the elastic modulus, as already demonstrated in continuous nanofibers, whose known size-dependent properties[42–45] are attributed to the molecular and supermolecular structure of the polymer matrix[18]. Such size tuning, combined with the possible biaxial nonuniform nanostructure, may find interesting applications in tissue engineering,[46] drug delivery, composites reinforcement, filtration, electrical and thermal conduction, and light amplification.

APPENDIX A: VISCOSITY MEASUREMENT

To determine the overlap concentration c^* and the entanglement concentration c_e for each molar mass, the solution specific viscosity was measured as a function of the polymer concentration (Fig. A1). The c^* and c_e (Table 2) were measured by intersecting the slopes of the three known concentration regimes, and compared well with c^* estimated from the measured intrinsic viscosity, $c^*=[\eta]^{-1}$, and with the literature[6]. The individual curves of each molar mass were normalized by their corresponding c_e and collapsed into a universal curve as a function of ϕ/ϕ_e (Fig. A1), where the mass concentration c was substituted by the dimensionless volume fraction $\phi=c/\rho$. The measured slopes were 1.1, 2.0, and 4.5 for the dilute, semidilute unentangled, and semidilute entangled regimes, respectively, close to both theoretical[14] (1, 2 and 4.7 for θ-solvent and 1, 1.3 and 3.9 for good solvent) and experimental values.[6]

APPENDIX B: EFFECT OF NETWORK DEFORMATION ON VISCOSITY

The theoretical prediction does not account for the effects of network deformation, chain disentanglement, and solvent evaporation on the solution viscosity. These complex effects are not introduced in the current analysis, but are briefly

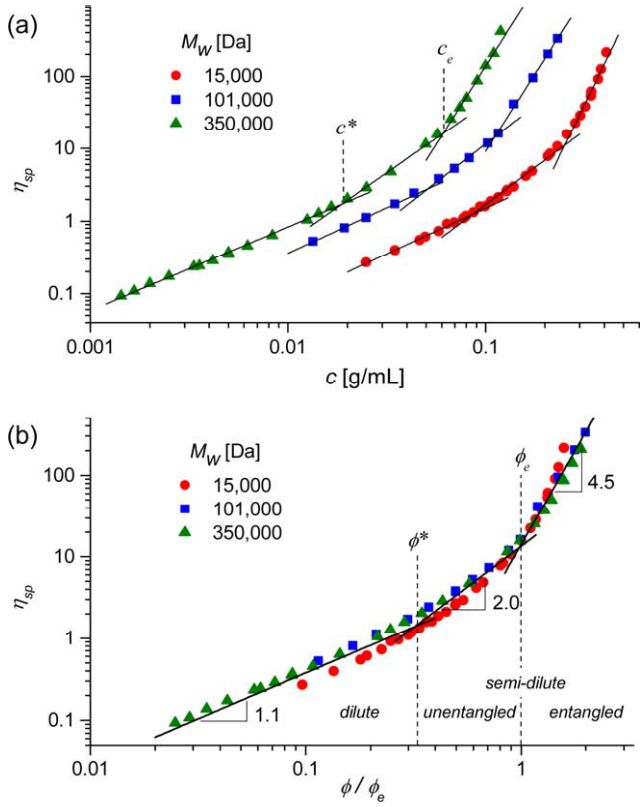

FIGURE A1 Measured specific viscosity, $\eta_{sp}=\eta/\eta_s-1$ (η and η_s are the solution and solvent viscosities, respectively), for PMMA dissolved in $CHCl_3$:DMF 50:50 vol % at 25 °C. (a) Viscosity *versus* solution concentration c. The concentration regimes were identified by power fit curves, the intersections of which provided the overlap concentration c^* and the entanglement concentration c_e for each molar mass. (b) Viscosity *versus* relative solution concentration ϕ/ϕ_e ($\phi=c/\rho$). The concentration regimes and the exponents of the power fit curves are indicated. [Color figure can be viewed in the online issue, which is available at wileyonlinelibrary.com.]

discussed below. The confining tube varies in consequence of the large network deformation and the rearrangement of chains and their interactions with neighboring chains. For example, the non-affine tube model of rubber elasticity predicts that the deformation dependence of the tube diameter is $a_{\mathrm{def}} \cong a\lambda^{1/2}$, where a is the undeformed tube diameter, and λ is the deformation factor.[47] When an entanglement strand, consisting of N_e monomers, approaches its full elastic extension, $\lambda \approx bN_e/(bN_e^{1/2}) \approx N_e^{1/2} \approx a/b \approx N_{e1}^{1/2}\phi^{-2/3}$ (θ-solvent), and therefore the deformed tube diameter increases by a factor of $\lambda^{1/2} \approx N_{e1}^{1/4}\phi^{-1/3}$. Since the dependence of the solution viscosity on the tube diameter is $\eta \sim a^{-4}$, the viscosity decreases by a factor of $\lambda^2 \approx N_{e1}\phi^{-4/3}$.

Further change is expected following the elongation of strands by disentanglement, which in turn decreases the viscosity by increasing the effective tube diameter. At the same time, the concurrent lateral network contraction, resulting from axial stretching,[18] may have an opposite effect because of a reduction in the deformation factor in the lateral direction. Also, while the longer chains in the population retain the continuity of the network, disentangled shorter chains effectively reduce viscosity. Finally, rapid evaporation, characteristic of electrospinning, increases the concentration and consequently the solution viscosity.

ACKNOWLEDGMENTS

The authors gratefully acknowledge the vital part of Dr. Ulrike Wangenheim in executing the short nanofibers experiment and the preliminary observations, and the valuable advice and support of Prof. Robert H. Schuster in planning the experiment, both from the Deutsches Institut für Kautschuktechnologie in Hannover, Germany. We thank Ron Avrahami from the Technion for assistance in carrying out the experiment. We acknowledge Dr. Arkadii Arinstein from the Technion for insightful discussions on polymer dynamics. We gratefully acknowledge the financial support of the United States-Israel Binational Science Foundation (BSF Grant 2006061), the RBNI−Russell Berrie Nanotechnology Institute, and the Israel Science Foundation (ISF Grant 770/11).

REFERENCES AND NOTES

1 C. J. Luo, E. Stride, S. Stoyanov, E. Pelan, M. Edirisinghe, *J. Polym. Res.* **2011**, *18*, 2515–2522.

2 A. Sutti, T. Lin, X. G. Wang, *J. Nanosci. Nanotechnol.* **2011**, *11*, 8947–8952.

3 K. Mukhopadhyay, C. D. Dwivedi, G. N. Mathur, *Carbon* **2002**, *40*, 1373–1376.

4 S. L. Shenoy, W. D. Bates, H. L. Frisch, G. E. Wnek, *Polymer* **2005**, *46*, 3372–3384.

5 S. Megelski, J. S. Stephens, D. B. Chase, J. F. Rabolt, *Macromolecules* **2002**, *35*, 8456–8466.

6 P. Gupta, C. Elkins, T. E. Long, G. L. Wilkes, *Polymer* **2005**, *46*, 4799–4810.

7 A. J. Guenthner, S. Khombhongse, W. X. Liu, P. Dayal, D. H. Reneker, T. Kyu, *Macromol. Theory Simul.* **2006**, *15*, 87–93.

8 A. Arinstein, E. Zussman, *Phys. Rev. E* **2007**, 76.

9 U. Stachewicz, R. J. Bailey, W. Wang, A. H. Barber, *Polymer* **2012**, *53*, 5132–5137.

10 Available at: www.surface-tension.de. **2006**, accessed on February 2013.

11 Available at: http://www.smartmeasurement.com. 2001–2002, accessed on February 2013.

12 J. E. Mark, Physical Properties of Polymers Handbook; AIP Press: Woodbury, N.Y., **1996**.

13 M. Selvakumar, D. K. Bhat, N. G. Renganathan, *J. Appl. Polym. Sci.* **2009**, *111*, 452–460.

14 M. Rubinstein, R. H. Colby, Polymer Physics; Oxford University Press: Oxford; New York, **2003**.

15 G. Taylor, *Proc. R. Soc. London Ser. A: Math. Phys. Sci.* **1966**, *291*, 145–158.

16 H. L. Cox, *Br. J. Appl. Phys.* **1952**, *3*, 72.

17 A. Kelly, W. R. Tyson, *J. Mech. Phys. Solids* **1965**, *13*, 329–350.

18 I. Greenfeld, A. Arinstein, K. Fezzaa, M. H. Rafailovich, E. Zussman, *Phys. Rev. E* **2011**, *84*, 041806.

19 Y. H. Wen, C. C. Hua, *J. Rheol.* **2009**, *53*, 781–798.

20 L. A. Archer, *J. Rheol.* **1999**, *43*, 1617–1633.

21 D. W. Mead, R. G. Larson, M. Doi, *Macromolecules* **1998**, *31*, 7895–7914.

22 V. R. Mhetar, L. A. Archer, *J. Polym. Sci. Part B: Polym. Phys.* **2000**, *38*, 222–233.

23 W. W. Zuo, M. F. Zhu, W. Yang, H. Yu, Y. M. Chen, Y. Zhang, *Polym. Eng. Sci.* **2005**, *45*, 704–709.

24 M. M. Hohman, M. Shin, G. Rutledge, M. P. Brenner, *Phys. Fluids* **2001**, *13*, 2201–2220.

25 Y. M. Shin, M. M. Hohman, M. P. Brenner, G. C. Rutledge, *Polymer* **2001**, *42*, 9955–9967.

26 E. Zussman, D. Rittel, A. L. Yarin, *Appl. Phys. Lett.* **2003**, *82*, 3958–3960.

27 H. Fong, I. Chun, D. H. Reneker, *Polymer* **1999**, *40*, 4585–4592.

28 H. Fong, D. H. Reneker, *J. Polym. Sci. Part B: Polym. Phys.* **1999**, *37*, 3488–3493.

29 D. H. Reneker, A. L. Yarin, H. Fong, S. Koombhongse, *J. Appl. Phys.* **2000**, *87*, 4531–4547.

30 I. Greenfeld, K. Fezzaa, M. H. Rafailovich, E. Zussman, *Macromolecules* **2012**, *45*, 3616–3626.

31 V. N. Kirichenko, I. V. Petrianovsokolov, N. N. Suprun, A. A. Shutov, *Doklady Akademii Nauk SSSR* **1986**, *289*, 817–820.

32 A. F. Spivak, Y. A. Dzenis, *Appl. Phys. Lett.* **1998**, *73*, 3067–3069.

33 M. M. Hohman, M. Shin, G. Rutledge, M. P. Brenner, *Phys. Fluids* **2001**, *13*, 2221–2236.

34 F. J. Higuera, *J. Fluid Mech.* **2006**, *558*, 143–152.

35 S. N. Reznik, E. Zussman, *Phys. Rev. E* **2010**, *81*, 026313.

36 A. Theron, E. Zussman, A. L. Yarin, *Nanotechnology* **2001**, *12*, 384–390.

37 S. Y. Gu, J. Ren, *Macromol. Mater. Eng.* **2005**, *290*, 1097–1105.

38 M. G. McKee, G. L. Wilkes, R. H. Colby, T. E. Long, *Macromolecules* **2004**, *37*, 1760–1767.

39 S. Kedem, J. Schmidt, Y. Paz, Y. Cohen, *Langmuir* **2005**, *21*, 5600–5604.

40 S. Kidoaki, K. Kwon, T. Matsuda, *J. Biomed. Mater. Res. Part B: Appl. Biomater.* **2006**, *76B*, 219–229.

41 S. C. Baker, N. Atkin, P. A. Gunning, N. Granville, K. Wilson, D. Wilson, J. Southgate, *Biomaterials* **2006**, *27*, 3136–3146.

42 Y. Ji, C. Li, G. Wang, J. Koo, S. Ge, B. Li, J. Jiang, B. Herzberg, T. Klein, S. Chen, J. C. Sokolov, M. H. Rafailovich, *Europhys. Lett.* **2008**, *84*, 56002.

43 M. Burman, A. Arinstein, E. Zussman, *Appl. Phys. Lett.* **2008**, *93*, 193118.

44 A. Arinstein, M. Burman, O. Gendelman, E. Zussman, *Nat. Nanotechnol.* **2007**, *2*, 59–62.

45 E. Zussman, A. Arinstein, *J. Polym. Sci. Part B: Polym. Phys.* **2011**, *49*, 691–707.

46 R. Ravichandran, J. R. Venugopal, S. Sundarrajan, S. Mukherjee, R. Sridhar, S. Ramakrishna, *Nanotechnology* **2012**, 23.

47 M. Rubinstein, S. Panyukov, *Macromolecules* **2002**, *35*, 6670–6686.